Spatial distribution of intrinsic and scattering seismic attenuation in active volcanic islands – II: Deception Island images

Janire Prudencio,[1,2] Jesús M. Ibáñez,[1,2] Araceli García-Yeguas,[1]
Edoardo Del Pezzo[1,3] and Antonio M. Posadas[1,4]

[1]*Instituto Andaluz de Geofísica, Campus de Cartuja, University of Granada, E-18071 Granada, Spain. E-mail: jibanez@ugr.es*
[2]*Departamento de Física Teórica y del Cosmos, Universidad de Granada, E-18071 Granada, Spain*
[3]*Istituto Nazionale di Geofisica e Vulcanologia, Sezione di Napoli – Osservatorio Vesuviano, Via Diocleziano 328, I-80124 Napoli, Italy*
[4]*Departamento De Química y Física, Cañana de San Urbano, University of Almería, E-04071 Almería, Spain*

SUMMARY

In this work, we present regional maps of the inverse intrinsic quality factor (Q_i^{-1}), the inverse scattering quality factor (Q_s^{-1}) and total inverse quality factor (Q_t^{-1}) for the volcanic environment of Deception Island (Antarctica). Our attenuation study is based on diffusion approximation, which permits us to obtain the attenuation coefficients for every single couple source-receiver separately. The data set used in this research is derived from an active seismic experiment using more than 5200 offshore shots (air guns) recorded at 32 onshore seismic stations and four ocean bottom seismometers. To arrive at a regional distribution of these values, we used a new mapping technique based on a Gaussian space probability function. This approach led us to create '2-D probabilistic maps' of values of intrinsic and scattering seismic attenuation. The 2-D tomographic images confirm the existence of a high attenuation body below an inner bay of Deception Island. This structure, previously observed in 2-D and 3-D velocity tomography of the region, is associated with a massive magma reservoir. Magnetotelluric studies reach a similar interpretation of this strong anomaly. Additionally, we observed areas with lower attenuation effects that bear correlation with consolidated structures described in other studies and associated with the crystalline basement of the area. Our calculations of the transport mean-free path and absorption length for intrinsic attenuation gave respective values of ≈950 m and 5 km, which are lower than the values obtained in tectonic regions or volcanic areas such as Tenerife Island. However, as observed in other volcanic regions, our results indicate that scattering effects dominate strongly over the intrinsic attenuation.

Key words: Seismic attenuation; Seismic tomography; Volcano seismology; Wave scattering and diffraction; Wave propagation.

1 INTRODUCTION

There is increasing interest in the interpretation of velocity tomography images in active volcanoes, as they strongly contribute to constraining volcano dynamics. Recent results of this kind were achieved at Mount St Helens (Lees & Crosson 1989), Kilauea (Rowan & Clayton 1993), Vesuvius (Zollo *et al.* 1998), Etna (Patanè *et al.* 2006) and Azores (Zandomeneghi 2007; Zandomeneghi *et al.* 2008). These images reveal a general presence in volcanoes of strong lateral velocity contrasts, which may be associated with volcanoclastic deposits, multifractured media or the presence of fluids (hydrothermal or magmatic origin).

Despite the importance of the tomography images in volcanoes, achieving them remains a difficult task, as one prerequisite to obtain a stable and robust inversion is a seismic network with an optimal distribution of receivers, associated with a uniform distribution of

earthquake foci inside the volume under study. Because such an optimal scenario is rare, the structure of many volcanoes is still unknown. In recent years, this matter has been approached through active experiments where seismic signals are artificially generated on land or at sea. Examples in Japan include the Kirishima (e.g. Tomatsu *et al.* 2001), Unzen (e.g. Shimizu *et al.* 1997) and Usu volcanoes (Onizawa *et al.* 2007), the TomoVes experiment in Vesuvio (Gasparini *et al.* 1998), TOMODEC at Deception Island (Zandomeneghi *et al.* 2009), Tom-Teidevs at Tenerife (Ibáñez *et al.* 2008) or SEA-CALIPSO at Montserrat (Voight *et al.* 2010). On the other hand, one important limitation of active seismic studies is that they are based solely on the observation of the *P*-wave traveltimes, which cannot definitively confirm the presence of fluids in the case of low velocity anomalies.

This problem can be mitigated by complementary information coming from seismic attenuation, particularly useful for interpreting

volcano dynamics. An early effort to determine the scattering and attenuation parameters for volcanic environments entailed using the estimate of coda Q^{-1}, or Q_c^{-1} of the local volcano-tectonic (VT) earthquakes (Aki & Chouet 1975) in the assumption of single-scattering process. At present, the most complete approach to characterize volcanic environments in term of energy propagation, intrinsic attenuation and scattering properties is the radiative transfer theory (based on the transport equation), which involves multiple scattering of any order (Zeng et al. 1991; Ryzhik et al. 1996). This theory, which can be fitted to the experimental coda envelope to obtain the scattering and intrinsic attenuation coefficients, is often applied using multiple lapse-time window analysis (Hoshiba 1993). The transport equation has an important asymptotic approximation in the case of strong scattering: the diffusion equation (Wegler & Lühr 2001; Wegler 2003, 2004). This approximation is mathematically much simpler and can therefore be easily applied to real data. Work by Wegler & Lühr (2001) at Merapi volcano and La Rocca et al. (2001) at Mt Vesuvius, using small aperture seismic arrays, led them to justify the presence of diffusive waves in local seismograms in volcanic environments. These and other theoretical results, such as those reported by Aki (1992) or Yamamoto & Sato (2010), point to the utility of the separate analysis of intrinsic and scattering attenuation using seismic active data in volcanic areas by means of the diffusivity approach. Del Pezzo (2008) provides a thorough review of this matter.

Prudencio et al. (2013, this issue) present a new method to obtain 2-D maps of scattering and intrinsic attenuation. These authors apply the diffusion approximation of the transport equation to fit the energy envelope of seismograms, in order to estimate separately the effect of scattering and seismic attenuation at Tenerife Island (Canary Islands). This methodology was previously used by Wegler & Lühr (2001) and Wegler (2003) to fit the coda envelopes of local quakes occurring in other volcanoes. In this paper, we use data from an active experiment carried out at Deception Island (Zandomeneghi et al. 2009), and estimate two parameters (proportional to intrinsic- and scattering-attenuation coefficients) for any single seismogram envelope. The new means of deriving a map of the spatial distribution of these values through the introduction of a weighting function of the space of coordinates based on a Gaussian form

In recent years, Ben-Zvi et al. (2009), Barclay et al. (2009) and Zandomeneghi et al. (2009) presented results of 2-D profiles and 3-D *P*-wave velocity tomography using data from an active seismic experiment (TOMODEC) in the Deception Island volcano. The above authors found that the inner bay of the island is characterized by a very low velocity body that extends from the surface to the resolution limit; on the basis of numerical models and volcanological evidence, they interpret this body as a magmatic intrusion feeding the volcanic system. However, a certain degree of uncertainty underlies this interpretation, founded on the use solely of *P*-wave data.

In this work, we analyse the data set used by the above authors to derive a separate intrinsic and scattering attenuation structure. Our results provide further confirmation of the structural complexity of Deception Island volcano, including additional proof of the presence of a large molten body near the surface, located in the inner bay (Port Foster) of the island.

2 GEOLOGICAL AND GEOPHYSICAL SETTINGS

Deception Island is a strato-volcano located between the South Shetland Islands and the Antarctic Peninsula. Even though it is considered to be the most active volcano of the backarc of the Bransfield Strait, the origin, history and regional tectonic context of Deception Island is poorly understood. Some models propose that Deception Island suffered a major caldera-forming eruption, while others suggest that the inner flooded bay (Port Foster) formed progressively through passive extension along sets of normal faults that cut the island (Martí et al. 1996; Smellie et al. 2002). The emerged top of the volcano is a small horseshoe-shaped island with a diameter of ∼15 km that encircles the inner bay (Port Foster), with a narrow opening to the sea (Fig. 1). Most of the island is covered by glaciers, volcanic cones and lava flows. The volcanic activity extends from 0.75 Ma to the last eruptions in 1842, 1967, 1969 and 1970 (e.g. Baker et al. 1975; Smellie 2001).

The local seismicity of Deception Island is consistent with that of an active volcano. It includes VT earthquakes related to the activation of faults, as well as long-period events mostly related to the interactions between shallow aquifers and hot materials. Additionally, volcanic tremor, hybrid events, avalanche signals, rock falls and ice crack signals have been detected and analysed (Almendros et al. 1997; Ortiz et al. 1997; Alguacil et al. 1999; Ibáñez et al. 2000, 2003; Carmona et al. 2012).

Many seismic studies have demonstrated the structural complexity of the Deception Island volcano. Saccorotti et al. (2001) analysed the data from two short period seismic arrays deployed at the island, and found a complex wave field associated with the magmatic and hydrothermal activity of the volcano. They furthermore investigated the dispersive properties of the Rayleigh waves at both arrays to obtain a shallow velocity structure below both, showing strong differences. The velocity differences were attributed to the different fracture systems bordering the inner volcano structure. Recently, Luzón et al. (2011) completed this study for different seismic array sites at the inner corner of Deception Island. In addition to observing that the upper part of the island is made up of relatively soft volcanoclastic and sedimentary deposits extending about 400 m, they observed highly variable deeper structures most likely associated with pre-calderic structure and products. García-Yeguas et al. (2011) analysed data recorded by eight seismic arrays during an active seismic experiment to compare estimated array solutions with theoretical values where source and receiver positions are well known. They found strong differences between the two values (observed and expected), interpreted as the effects of the seismic wave propagation.

According to Ben-Zvi et al. (2009) and Zandomeneghi et al. (2009), the main feature of the tomographic images of Deception Island is the presence of a low-velocity body under Port Foster (Fig. 2), described as a possible shallow magmatic chamber surrounded by high-velocity chilled magmatic bodies and crystalline continental basement.

The presence of melt beneath Port Foster has also been inferred from seismic refraction studies (Somoza et al. 2004) and gravity, magnetism, magnetotelluric and seismic attenuation observations (Vila et al. 1995; Muñoz-Martin et al. 2005; Catalan et al. 2006; Pedrera et al. 2012).

3 DATA

In the present work, we analyse the data set provided by an active seismic experiment called TOMODEC, carried out in the Antarctic volcano of Deception Island during 2005 January. This data set was previously used to develop 2-D and 3-D velocity tomography and other studies of the region (Ben-Zvi et al. 2009; Zandomeneghi
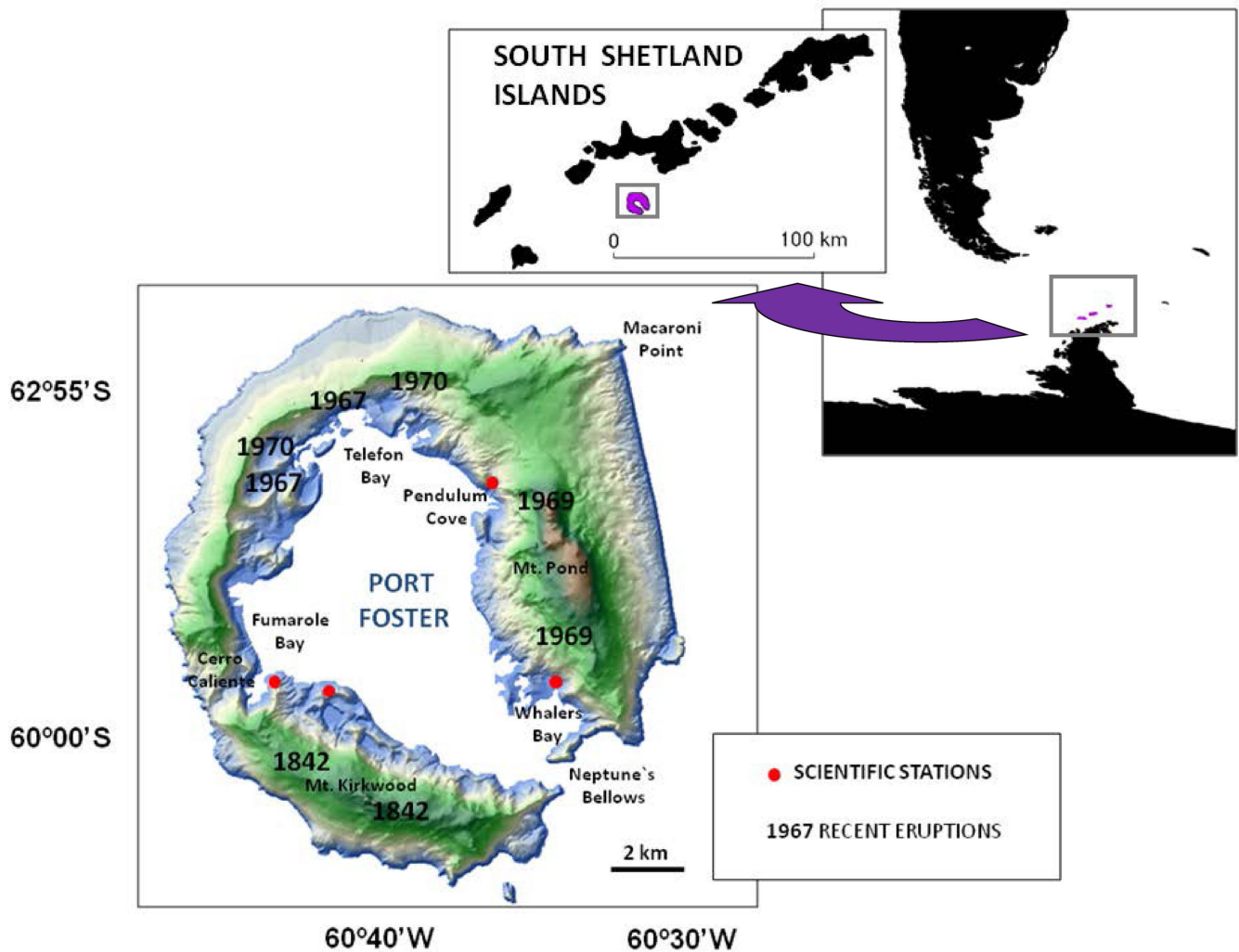
Figure 1. Geographic location of the South Shetland Islands and simplified topographic map of Deception Island, showing locations of last eruptions and scientific stations.

et al. 2009; García-Yeguas *et al.* 2011; Luzón *et al.* 2011). Seismic signals were generated by air gun shots fired on the sea and recorded at seismic stations distributed on the island and ocean bottom seismometers (OBS), as indicated in Fig. 3.

Air guns were placed aboard the Spanish Oceanographic research vessel *Hesperides*, using an array of six BOLT 1500LL air guns configured in pairs. The air gun arrays had a length of 12 m; the pairs of air guns were separated by 2.5 m, and the distance between pairs was 0.8 m. In the first round of shots in the inner bay only four guns were used with a total of 1520 cubic inches (24.91 l or 0.024908 m^3), while outside all of them were used 3520 cubic inches (57.7 l or 0.057 m^3). In the second round inside the bay, the total capacity was increased from 1520 to 2020 cubic inches (33.1 l or 0.033101 m^3). The signals were produced every minute in the inner bay of Deception Island and every 2 min offshore. The OBSs were distributed in the inner bay and in a circular configuration around the island. Onshore stations were installed at least 0.2 km far from the coastline covering the main part of the island, and included autonomous stations as well as dense seismic arrays with small distances in between, 100 to 300 m. During the experiment, some positions of the stations deployed on land and some of the OBS were changed in order to increase the number of places recording the seismic signals.

A total of 122 seismic stations on land and 14 OBS were deployed, and 1309 shots were performed in the inner bay of Deception Island and 3933 offshore. We used two types of onshore seismic stations configuration: we deployed 11 short aperture seismic arrays along Port Foster coast with 10–12 vertical seismic stations in each array and with a maximum separation of 300 m between seismometers; additional autonomous three-components seismometers were deployed in the inner part of Deception island. The quality of data is generally good, with a low noise level both on land and in some ocean bottom seismometers. Due to the nature of the emplacement site, cultural noise is completely absent, and the only observed effect is due to strong winds shaking the island coasts and the sporadic presence of volcanic tremor activity. OBS data sometimes have a signal to noise ratio lower than data collected on land, due to sea currents and other probable local sources of noise. Identifiable *P*-wave arrivals are recognized out to 30–40 km ranges and in some cases as far as 60 km. The distribution of the shots and seismic stations is shown in Fig. 3. Finally, we selected 32 stations on land and four OBS on the basis of the best signal quality (Fig. 4) and optimal spatial coverage. For onshore stations we selected from each seismic array only one or two high-quality stations as representative of the array site in order to avoid redundancies in data analysis, obtaining very good spatial coverage of the zone.
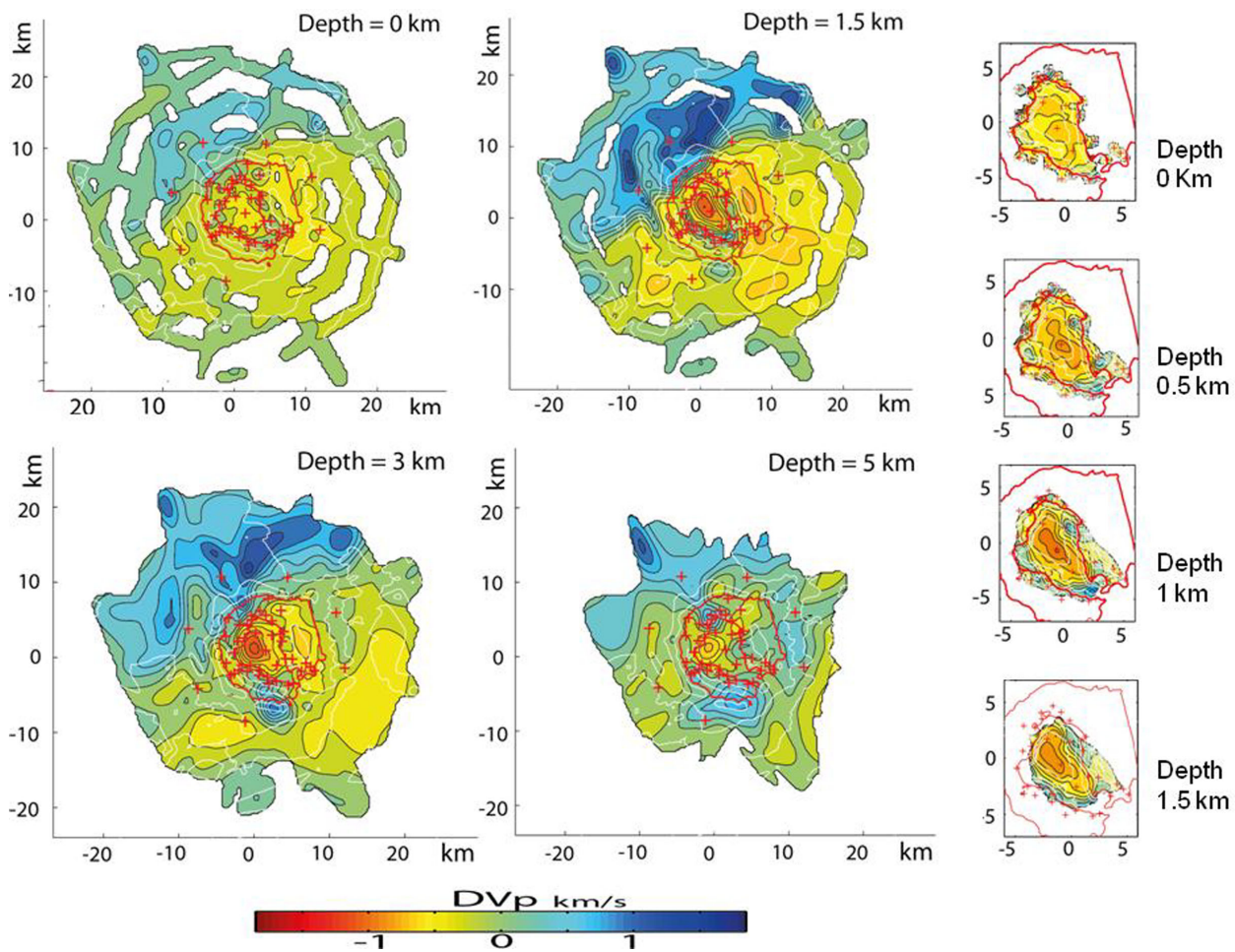
Figure 2. Tomographic images obtained by Zandomeneghi (2007) and Zandomeneghi *et al*. (2009). The images are horizontal sections at 0, 1.5, 3 and 5 km depth. In the right-hand part of the image, the area of the inner bay of Deception Island is shown at 0, 0.5, 1 and 1.5 km depth.
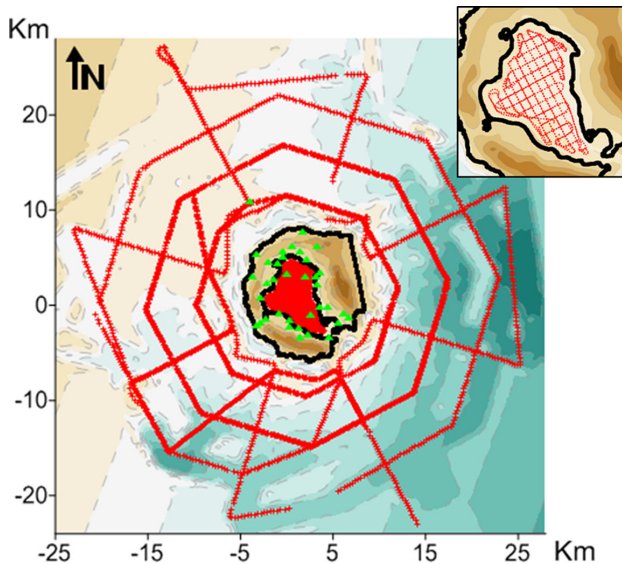
Figure 3. Map of Deception Island showing the experiment configuration. Positions of seismic stations (both land stations and ocean bottom seismometers, or OBS) are shown as green triangles (only the stations used in this work are shown) and the profile of air gun shots appears as red dots. Note that the inner bay of Deception Island is completely red due to the proximity of shots. The top right-hand part of the figure shows the configuration of the shot inside the inner bay.

4 METHOD AND DATA PROCESSING

We applied the methodology first developed by Wegler & Lühr (2001), applied by Wegler (2003) and Del Pezzo (2008) and described in Prudencio *et al*. (2013, this issue) to estimate separately the intrinsic and scattering attenuation coefficients.

The first step of the process is to fit observed to theoretical seismogram energy envelopes generated by the diffusion model, in terms of the intrinsic attenuation coefficient and diffusivity coefficient. This approach permits one to calculate the values of scattering and intrinsic attenuation coefficient for every seismogram associated to a single source–receiver couple. Filtering the observed seismogram in different frequency bands enabled us to study the frequency dependence of the two attenuation coefficients in the region.

First, spectral analysis was performed to determine the bandwidth where the seismic signal was recorded with a high signal-to-noise ratio (Fig. 4). In view of this analysis, we chose six frequency bands with central frequencies of 4, 6, 8, 12, 16 and 20 Hz.

The whole data analysis procedure was:

(i) *P*-wave onsets were taken from the work of Zandomeneghi *et al*. (2009) and the duration of the signal was measured in each seismogram, calculating the signal-to-noise ratio of the signals, fixing the end at the time when this ratio reached a value of 2.
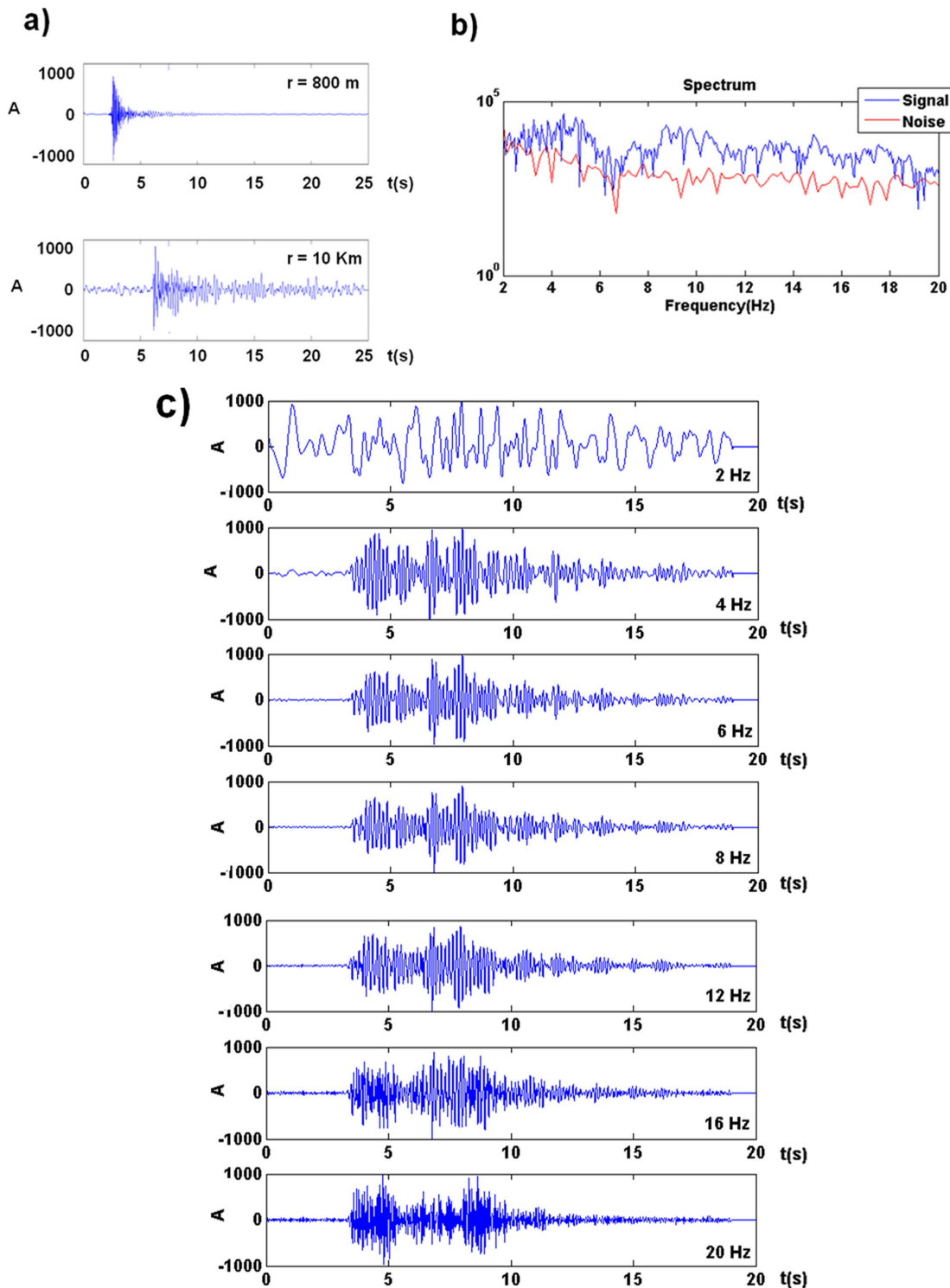
Figure 4. (a) An example of two Z-component seismograms of shots recorded at 800 m and 10 km from the station, filtered between 2 and 30 Hz. (b) Spectra of the seismogram of 10 km. The signal is plotted as a blue line and the prevent seismic noise as a red line. (c) The vertical component seismogram for an explosion recorded at 4.5 km from the source filtered at 4, 6, 8, 12, 16 and 20 Hz using an eight pole bandpass filter.

(ii) The signals were then filtered using an eight pole zero shift Butterword bandpass filter with central frequencies of 4, 6, 8, 12, 16 and 20 Hz and a bandwidth of $f_c \pm 0.6 f_c$ (Fig. 4).

(iii) Energy envelopes were calculated through Hilbert transform, using moving windows of a size of 70 samples (0.7 s long) over-

lapped 50 per cent. In Fig. 5 we show an example of the final envelope derived from the real data.

(iv) The squares of the envelopes are windowed between the *P*-wave arrival (t_{min}) and 15 s starting from the origin time (t_{max}).
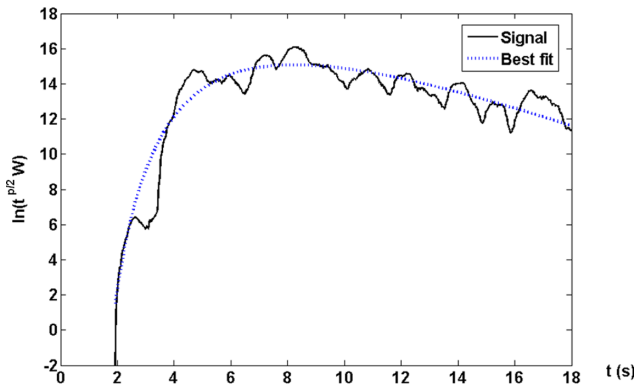
Figure 5. An example of the best fitting for observed energy envelope (black line) and theoretical curve (dashed blue line) for the logarithmic energy density.

(v) After multiplying by $t^{p/2}$ we fit $\mathrm{Log}(t^{p/2}\,W)$ to the corresponding theoretical quantity, retrieving a_1, a_2 and a_3 (eq. 4 from Prudencio *et al.* 2013) and hence b and d by:

$$b = -a_2 \tag{1}$$

$$d = -\frac{r^2}{4a_3}$$

(vi) We estimate Q_i and Q_s by:

$$Q_i = \frac{2\pi f}{b}, \tag{2}$$

$$Q_s = \frac{2\pi f p d}{v^2}, \tag{3}$$

where f is the frequency, p is the dimension (three in the assumption of the analysis of body waves) and v is the velocity for S waves, here taken as $v = 2.8\,\mathrm{km\,s^{-1}}$.

(vii) Following Mayeda *et al.* (1992) and Akinci *et al.* (1995), we used the F distribution at a 70 per cent level of confidence to estimate the uncertainty intervals in b and d parameters. We measured this uncertainty interval (and in parallel observed the potential trade-off between the two parameters b and d) plotting the rms of the estimates in a 2-D plot (an example is shown in Fig. 6). Percent uncertainty
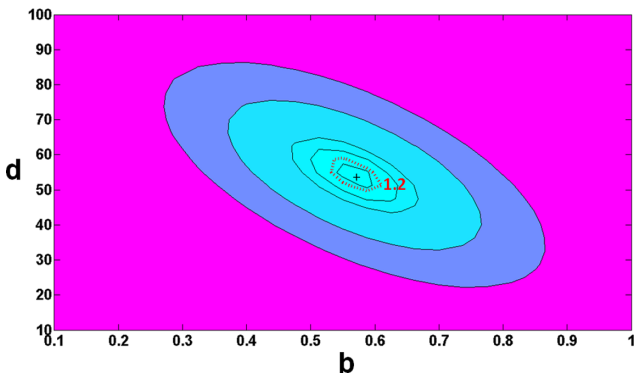
Figure 6. An example of the grid-search result for the fitting of experimental and theoretical energy envelope to obtain b and d attenuation parameters. The best fit corresponds to the paired values marked with a cross. Observe the absence of trade-off between parameters b and d; therefore, we can mate the two attenuation coefficients independently. Each ellipse surrounding the best fit corresponds to iso-surfaces with the same F distribution at a different per cent value. Dashed red line is associated to a 70 per cent level of confidence that permits us to estimate the uncertainty intervals.

intervals are $\Delta a_2 = \pm 7$ and $\Delta a_3 = \pm 9$ (eq. 5 from Prudencio *et al.* 2013). From the isolines of the error function observed in Fig. 6, we can deduce that the trade-off between b and d is minimal.

(viii) Then we calculated the uncertainty interval for the inverse of quality factors using the error propagation theory:

$$\Delta Q_i^{-1} = \frac{\sigma b}{2\pi f}, \tag{4}$$

$$\Delta Q_s^{-1} = \frac{4v^2\sigma c}{6f\pi r^2}. \tag{5}$$

(ix) Finally, we calculated the value of Q_t^{-1} as:

$$Q_t^{-1} = Q_i^{-1} + Q_s^{-1}. \tag{6}$$

Assuming a dominance of S waves, we can calculate the transport mean-free path, l_{tr} Given the results from Ben-Zvi *et al.* (2009) and Zandomeneghi *et al.* (2009), we took an average S-wave velocity (v) of 2.8 km s^{-1}. Using an average value of $d \approx 0.8\,\mathrm{km^2\,s^{-1}}$, we obtained $l_{tr} = 3d/v \approx 950\,\mathrm{m}$. This value is approximately two orders of magnitude smaller than usual values for the Earth's Crust (≈ 100 km). A comparison with values obtained in other regions [e.g. Merapi (≈ 100 m), Vesuvius (≈ 200 m) or Tenerife (≈ 4 km)], shows that the average heterogeneity at Deception is of the same order of Vesuvius and Merapi volcanoes, and significantly different from that measured in Tenerife. The absorption length for intrinsic attenuation, $l_i = v/b$, is of the order of ≈ 5 km, much larger than the transport mean-free path. This confirms that the scattering attenuation dominates over intrinsic attenuation.

5 RESULTS

5.1 New 2-D probabilistic attenuation maps

For the present work, we implemented a new mapping procedure of the attenuation parameters described by Prudencio *et al.* (2013). This process assumes that the majority of the seismogram is generated through diffusion processes in an area around the direct ray path between source and receiver. On these premises we can assign a maximum probability of occurrence of this diffusion process in the midpoint source–receiver region, assigning non-zero probability in the surrounding areas defined by an ellipsoid. Outside this ellipsoid the probability is zero. Thus, we can define a bidimensional Gaussian function centred at that midpoint region, which extends over a surface associated with source–station distance. For each source–receiver pair we estimated the values of Q_i and Q_s. Additionally, with the information of the distance source–receiver and the lapse time of the seismogram analysed, we built the ellipsoid following Prudencio *et al.* (2013). The region under study can be divided into cells, assigning to each one the different attenuation values weighted by the probability for each source–receiver pair analysed. At the end of the analytical procedure we will average all the attenuation values that have been assigned to each cell, to obtain the average Q_i and Q_s values of the entire data set analysed.

To elaborate regional attenuation maps, we divided the region into cells of 1 km × 1 km. The depth at which we obtained information is conditioned by the size of the minor semi-axes; in our case, 6 km deep on the average. Because we cannot invert the probabilistic function in depth, the final images are a projection at surface (2-D maps) of the attenuation phenomena occurring in the fixed 3-D volume. The surface projection of the different revolution ellipsoids was moved along the surface of the area under study in view of the position of the shots and receivers.

5.2 Resolution and robustness test

To check the resolution of the method, we performed a checkerboard test. The region was divided into cells of 3 km × 3 km and in 1 km × 1 km as shown in Fig. 6. In this figure, the test for a grid size of 1 km × 1 km is shown only for a small region to demonstrate the resolution of the method. We assigned values of *b* and *d* (in eq. 2 from Prudencio *et al.* 2013) for each cell; then, for each source–receiver couple, we calculated the average, weighted by a Gaussian function of the parameters *b* and *d* as described in Prudencio *et al.* (2013). The theoretical envelope is thus calculated using *b* and *d*, and finally, random noise is added.

These synthetic envelopes are fitted to the theoretical curves to obtain the checkerboard image (results shown in Fig. 7). We performed this test for both intrinsic (Figs 7a and b) and scattering attenuation (Figs 7c and d). As can be seen, there is good resolution for the entire region under study.

To test the robustness of the data we applied a jackknife test, randomly removing a percentage of data and stations. Fig. 8 shows the images with 100, 80 and 60 per cent of the data. It is evident that the main attenuation characteristics are maintained even with a loss of 40 per cent of the data.

5.3 Regional distribution of intrinsic and scattering attenuation

In Figs 9 and 10, we represent the regional distribution of Q_i^{-1} and Q_s^{-1} values, respectively. The following common patterns are seen:
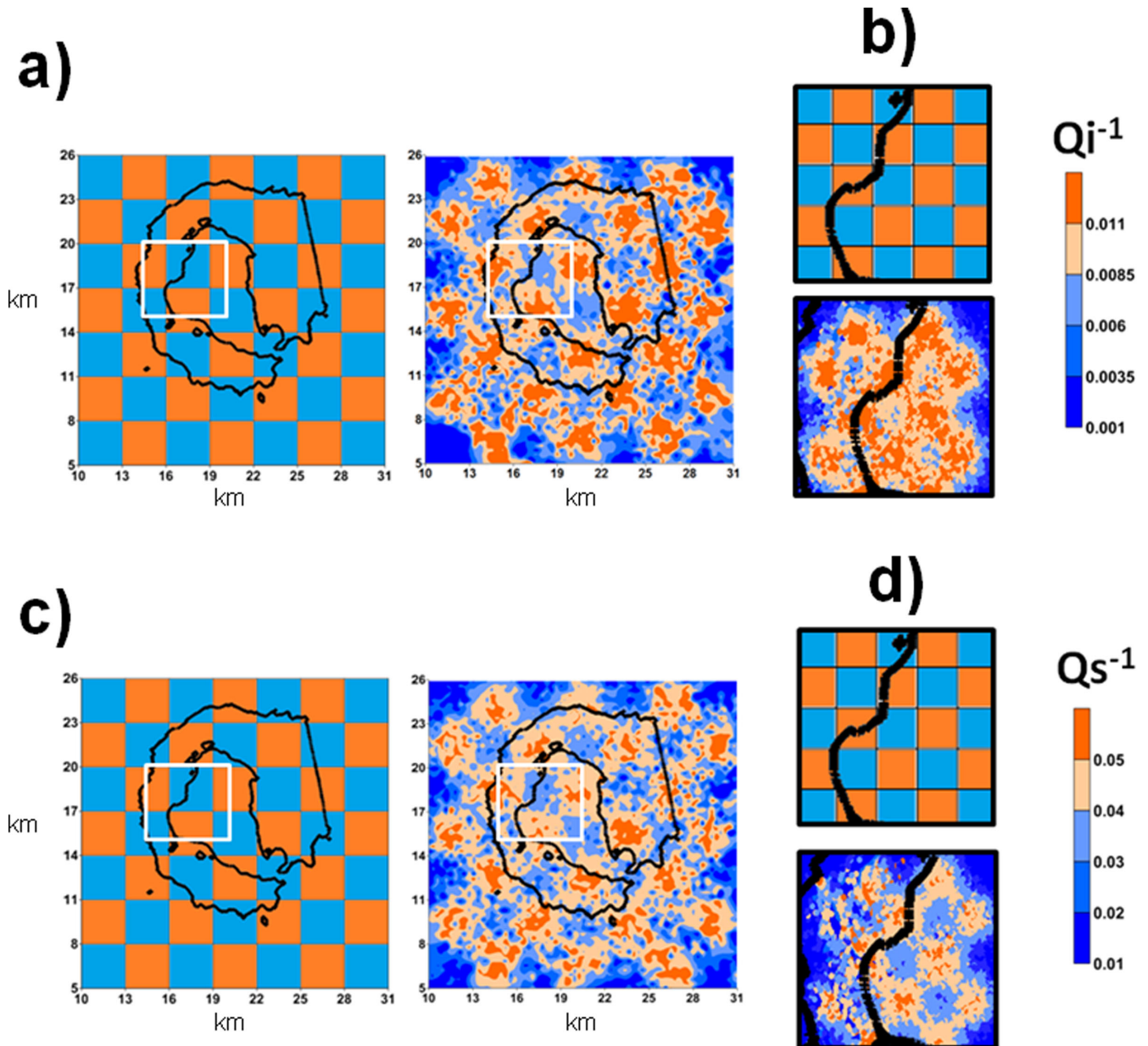
Figure 7. Checkerboard test for Deception Island. (a) The island is divided into 3 km × 3 km cells, different values of *b* and *d* are assigned to each cell and the obtained values of Q_i^{-1} are represented. (b) Results are shown for a smaller region of the island divided into 1 km × 1 km cells. (c) and (d) are the same as (a) and (b) but for Q_s^{-1} values.
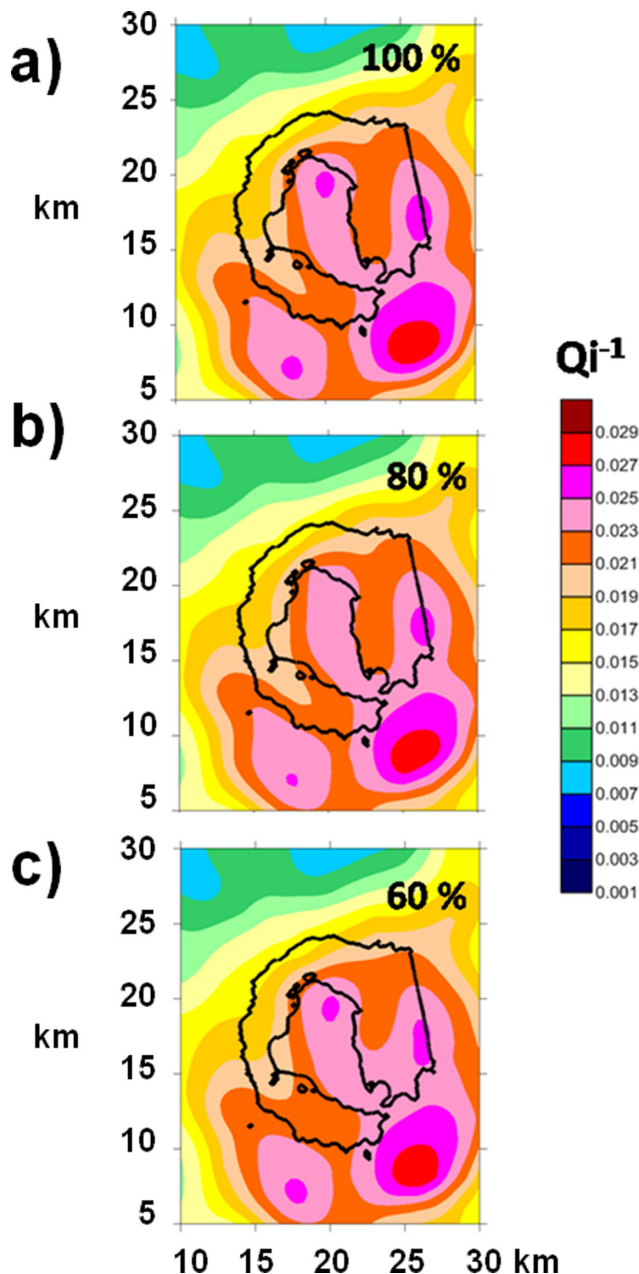
Figure 8. Jackknifing test images. The figure shows the images with 100 per cent (a), 80 per cent (b) and 60 per cent (c) of the data.

(i) The distribution of *Q* values reveals a very heterogeneous structure of the island.

(ii) *Q* is strongly frequency dependent.

The dominant attenuation process corresponds to scattering phenomena, as has been observed in other volcanic regions.

To highlight the local differences in the parameter under study, we calculated intrinsic and scattering inverse quality factor anomaly maps. This anomaly is defined as the difference between the value of the parameter that is obtained and the average value of this parameter in the whole region. Figs 11 and 12 illustrate the estimated anomaly map for Deception Island for intrinsic and scattering Q^{-1}, respectively, at the six frequency bands analysed. These maps were calculated using as baseline the average Q^{-1} value reported in Table 1.

6 DISCUSSION

In this work, we applied a method based on whole-seismogram fit to a diffusion model, in order to determine the spatial distribution of seismic intrinsic and scattering attenuation of the volcanic island of Deception. We use the procedure developed by Wegler & Lühr (2001) to fit the data derived from an active seismic experiment in the region. The regional distribution of the attenuation values obtained for Deception Island, as a function of frequency, is shown in Figs 9 and 10.

6.1 Average intrinsic and scattering *Q* values and their frequency dependence

The average *Q* value for the entire region as a function of the frequency is given in Table 1. A strong dependence between *Q* and frequency (for both Q_i and Q_s) is observed. The empirical relationships linking inverse-Q and frequency are: $Q_i = 19 \times f^{0.85}$, $Q_s = 3 \times f^{0.87}$ and $Q_t = 9 \times f^{0.93}$.

Note that the three average *Q* values have very similar frequency dependence, from 0.85 to 0.93. This range is in line with the frequency dependence observed in several volcanic regions (e.g. Sato & Fehler 1998, p. 196; Del Pezzo 2008). If we compare the present results to other attenuation estimates obtained for the same region (e.g. Vila *et al.* 1995 or Martínez-Árevalo *et al.* 2003) we observe similar pattern. Moreover, the present Q_i values are very close to other attenuation estimates of Q_i and similar to the Q_c, reported for other regions (Del Pezzo 2008). Other previous authors such as Martínez-Árevalo *et al.* (2003) obtained a frequency dependence law of $Q_i = 15 \times f^{0.86}$ while Q_c at a lapse time of 8 s followed a frequency pattern given by $Q_c = 12 \times f^{0.88}$ for a lapse time of 10 s $Q_c = 24 \times f^{0.70}$. It is noteworthy that different data and techniques provide very similar intrinsic attenuation values. In general, the most significant correlations in the different attenuation studies of the region are:

(i) Strong seismic attenuation.
(ii) Strong dependence of the attenuation with frequency.
(iii) Strong predominance of scattering attenuation over the intrinsic attenuation.

It is remarkable that scattering effects clearly predominate over the intrinsic attenuation, with Q_s values an order of magnitude lower than Q_i estimations. Even in the external areas of the island, where the effects of scattering are lower, its contribution to total-*Q* is more important than the contribution of intrinsic attenuation.

6.2 Regional distribution of Q_i^{-1}

Fig. 9 shows how a very heterogeneous distribution of intrinsic attenuation values characterizes the investigated area. We interpret this heterogeneity in terms of tectonic and volcanic properties of the region, in light of the Fig. 7 from Zandomeneghi *et al.* (2009) and Figs 6 and 7 from Ben-Zvi *et al.* (2009). Two clearly different regions can be distinguished in Fig. 9 of this paper in terms of their intrinsic attenuation behaviour: the upper North zone of the region, which presents very-low attenuation values, and the rest of the zone where high intrinsic attenuation bodies are identified together with other small low intrinsic attenuation structures. It is remarkable that in the areas where Ben-Zvi *et al.* (2009) and Zandomeneghi *et al.* (2009) observed high velocity anomalies, we found low intrinsic attenuation values (high Q_i), and vice versa; thus, we associate
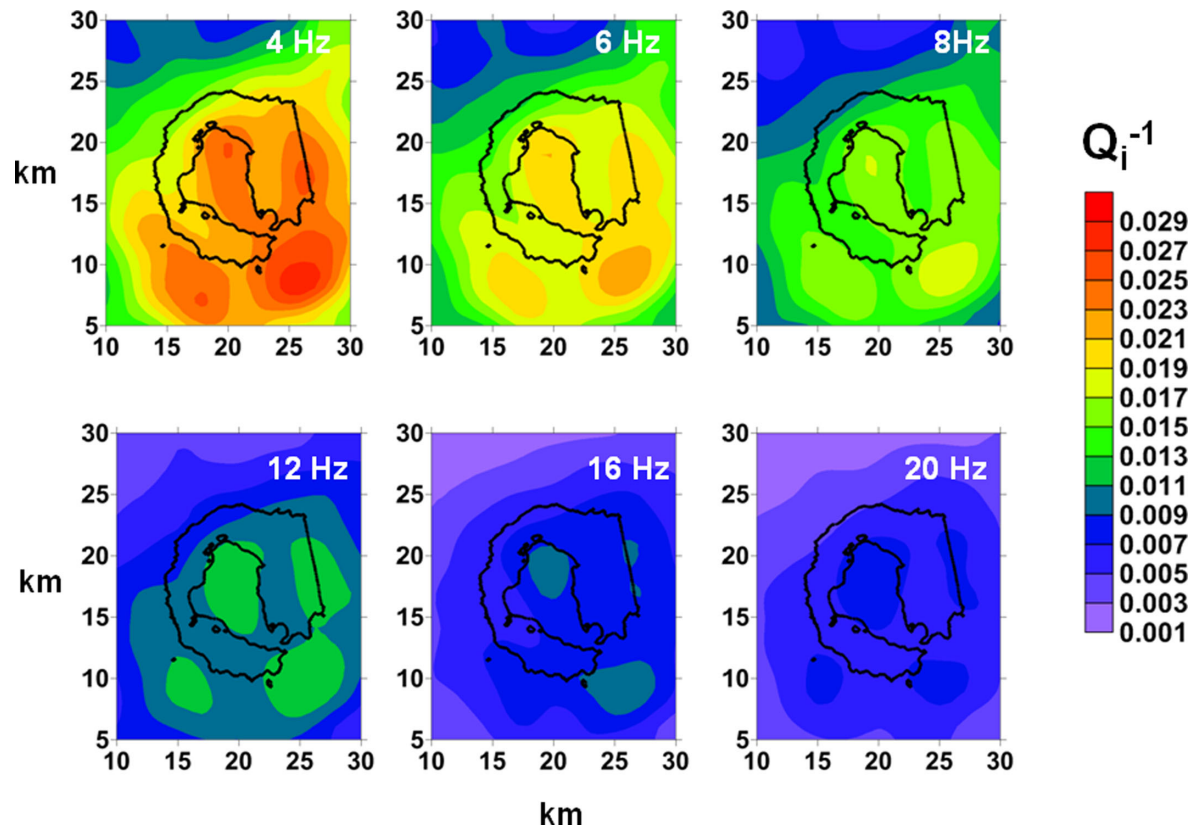
Figure 9. Regional map of Q_i^{-1} obtained with the probabilistic Gaussian representation method for the six frequency bands analysed. A, B, C and D correspond to high intrinsic attenuation areas described in Section 6.2.

areas with high attenuation values with those characterized by low velocity anomalies.

This Northern region, with low intrinsic attenuation values, matches the crystalline basement of the continental edge of the Bransfield Strait. As Zandomeneghi *et al.* (2009) indicate, this area should be more consolidated and rigid than the Southern part of the studied area. This region, defining the northwestern limit of the Bransfield Basin, coincides with the northern margin of the caldera, likewise confirmed by bathymetric studies (Barclay *et al.* 2009).

There are four well-defined high intrinsic attenuation zones identified as A, B, C and D in Fig. 9. All of them match zones of low velocity anomalies determined by Zandomeneghi *et al.* (2009). Each high intrinsic attenuation area was interpreted according to different structural and volcanological characteristics by Ben-Zvi *et al.* (2009) and Zandomeneghi *et al.* (2009). Three high intrinsic attenuation areas are located outside Deception Island and one of them (zone A) just beneath Port Foster in the centre of the Island. The high intrinsic attenuation area of Port Foster matches an area identified by the above authors as a large magma chamber below Deception Island extending from 1 km depth to the limit of resolution of their studies (around 8 km depth). However, the effect of a thick shallow sedimentary layer located from the surface to around 1.5 km depth (Ben-Zvi *et al.* 2009) cannot be excluded.

Our high intrinsic attenuation areas B and C can be interpreted as a combination of different factors such as: strong sedimentary deposits, the presence of evident active normal faulting systems (Fernandez-Ibáñez *et al.* 2005) and the existence of several slump deposits and channels, and some possible volcanic seamounts

(Barclay *et al.* 2009). The high intrinsic attenuation observed in region D could be related to the presence of a rougher seafloor that includes small seamounts due to a possibly thicker extrusive layer (Barclay *et al.* 2009; Zandomeneghi *et al.* 2009).

## 6.3 Regional distribution of Q_s^{-1}

Since the scattering process predominates over the intrinsic attenuation, with differences of an order of magnitude, total-Q distribution is practically identical to scattering.

The main observation is that an area with the strongest scattering effect in comparison to the rest of the studied region corresponds to the centre of Deception Island (Port Foster). This coincides with region A of the intrinsic attenuation maps. Interestingly, the high scattering anomaly is maintained for all frequency ranges analysed. This observation implies that the scattering effect is present for the entire wavelength range. As indicated in the interpretation of Q_i, this particular region is located in a zone where previous studies reported a layer of low-velocity material infilling the caldera basin along with an underlying possible magma chamber extending downward from around 1.5 km below the seafloor to as much as 6 km, which may contain a large volume of molten material (Ben-Zvi *et al.* 2009; Zandomeneghi *et al.* 2009).

The fact that we observed such strong scattering attenuation contrast associated with the area where the presence of magma is confirmed could suggest that the melt zone is not homogeneous, possibly formed by the superposition of melt pockets inside a structure formed by colder rocks, thus favouring the scattering of the shear waves.
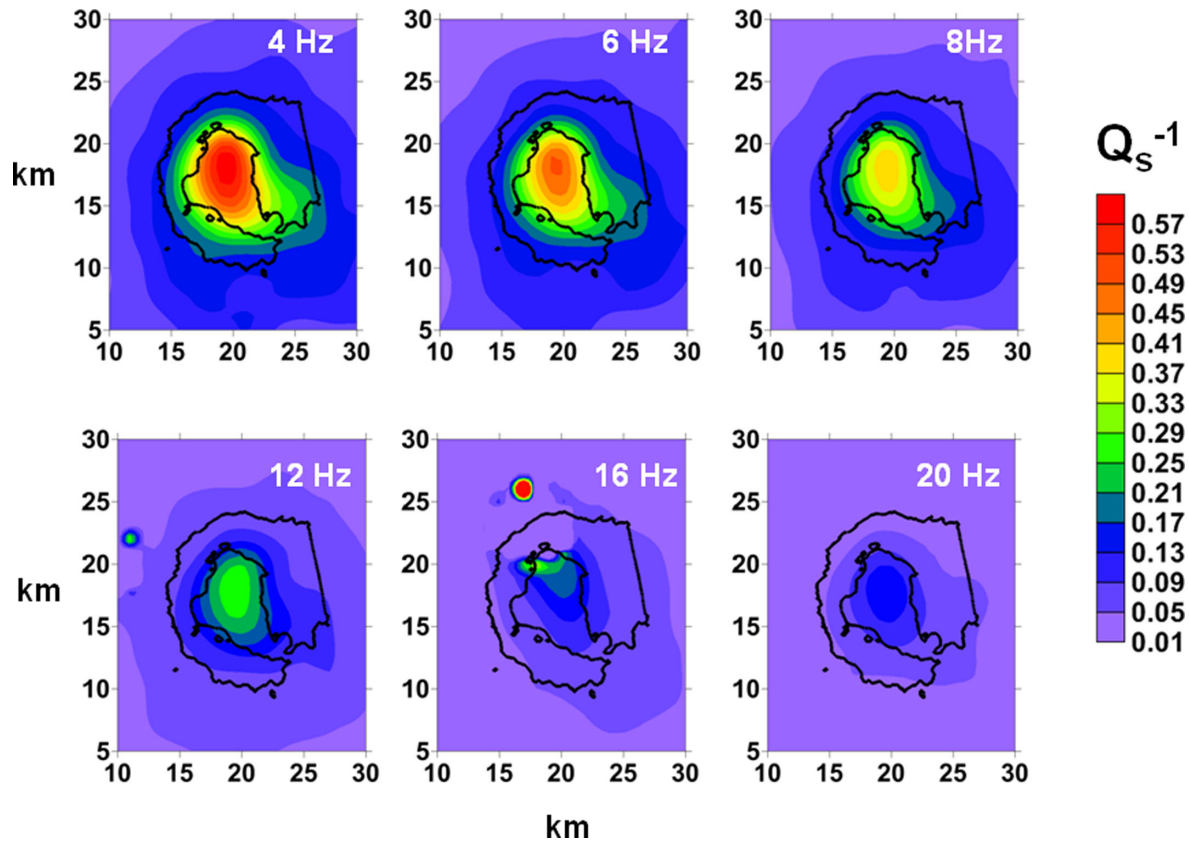
Figure 10. Regional map of Q_s^{-1} obtained with the probabilistic Gaussian representation method for the six frequency bands analysed. Note that scattering values are at least two orders of magnitude greater than intrinsic values. These high values indicate that the scattering effect predominates over intrinsic attenuation.
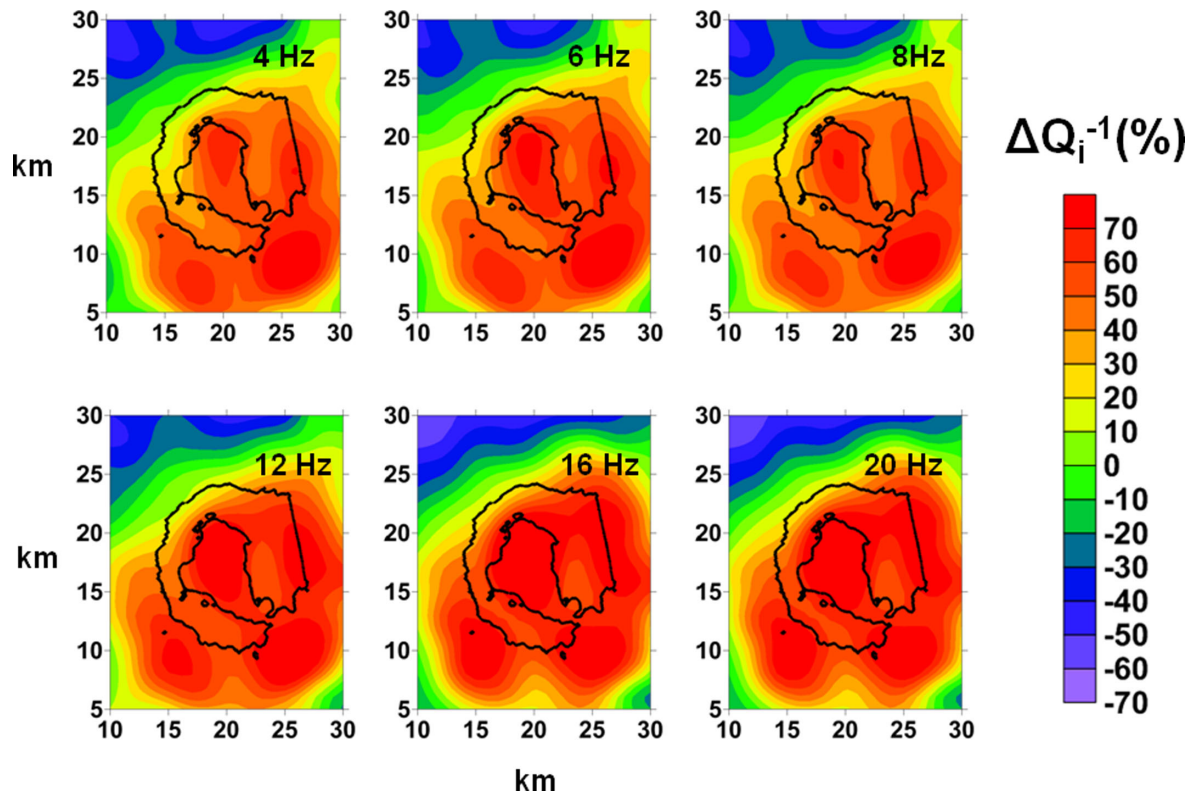
Figure 11. Q_i^{-1} anomaly maps for the six frequency band analysed, highlighting the areas with strongest attenuation contrast.
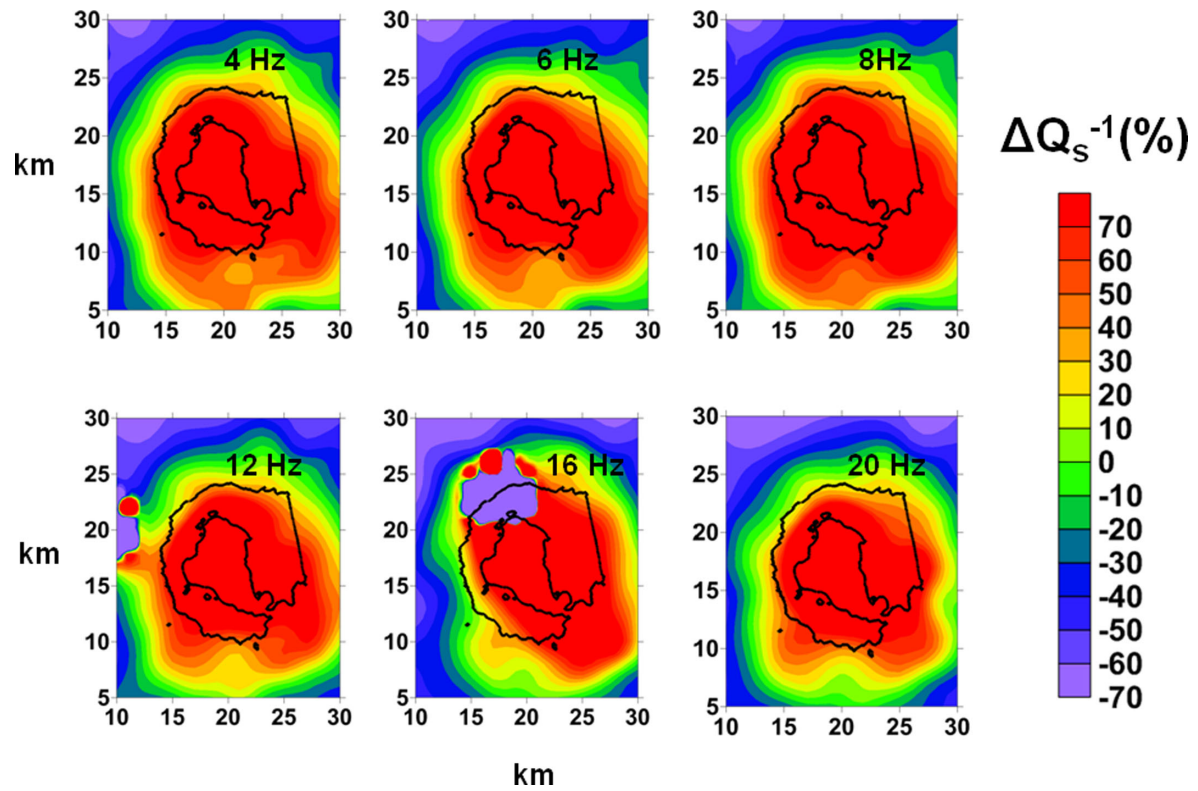
Figure 12. Q_s^{-1} anomaly maps for the six frequency band analysed, highlighting the central area of the island with the strongest scattering attenuation contrast.

Table 1. Average values of Q_i^{-1}, Q_s^{-1} and Q_t^{-1} and Q_i, Q_s and Q_t.

Frequency (Hz)	Q_i^{-1}	Q_s^{-1}	Q_t^{-1}	Q_i	Q_s	Q_t
4	0.015 ± 0.002	0.09 ± 0.03	0.11 ± 0.03	67	11	9
6	0.012 ± 0.001	0.08 ± 0.02	0.09 ± 0.02	83	12	11
8	0.010 ± 0.001	0.06 ± 0.01	0.07 ± 0.01	100	17	14
12	0.0066 ± 0.0007	0.044 ± 0.009	0.051 ± 0.009	151	23	20
16	0.0048 ± 0.0005	0.030 ± 0.006	0.032 ± 0.006	208	33	31
20	0.0040 ± 0.0004	0.024 ± 0.005	0.026 ± 0.005	250	42	38

6.4 Regional distribution of anomalies of Q_i^{-1} and Q_s^{-1}

The maps highlight areas with strong contrast in attenuation. In the case of intrinsic attenuation, the four defined zones with high attenuation effects are more clearly emphasized. For scattering attenuation, we see the effect of the high attenuation at the centre of the island. In any case, the attenuation contrast of the island is very high, as indicated in the distribution of the Q anomaly values.

7 CONCLUSIONS

This paper presents a study of the distribution of intrinsic and scattering attenuation for the volcanic island of Deception. Assuming the dominance of S waves and S-wave velocity (v) of $2.8\,\mathrm{km\,s^{-1}}$, we measured a transport mean free path of $l_{tr} = 3d/v \approx 950\,\mathrm{m}$. This result is two orders of magnitude smaller than values calculated for the usual crust of the Earth ($l_{tr} \approx 100\,\mathrm{km}$). We arrived at a typical absorption length for intrinsic attenuation of $l_i = v/b$. We obtain values around $5\,\mathrm{km}$. These results confirm that the attenuation of the direct S waves in Deception Island is predominantly caused by scattering rather than by intrinsic attenuation, in agreement with previous attenuation studies of volcanic regions.

The spatial distribution of the stations and sources allowed us to obtain a robust and reliable 2-D image of Deception Island that reveals the existence of a strong contrast of the attenuative behaviour in the region, probably related (in view of the findings by Ben-Zvi *et al*. 2009; Zandomeneghi *et al*. 2009; Pedrera *et al*. 2012) to the presence of a large magmatic volume near the surface.

REFERENCES

Aki, K., 1992. Scattering conversion P to S versus S to P, *Bull. seism. Soc. Am.,* **82,** 1969–1972.

Aki, K. & Chouet, B., 1975. Origin of coda waves: source, attenuation and scattering effects, *J. geophys. Res.,* **80,** 3322–3342.

Akinci, A., Del Pezzo, E. & Ibáñez, J., 1995. Separation of scattering and intrinsic attenuation in southern Spain and western Anatolia (Turkey), *Geophys. J. Int.,* **121,** 337–353.

Alguacil, G., Almendros, J., Del Pezzo, E., García, A., Ibáñez, J.M., La Rocca, M., Morales, J. & Ortiz, R., 1999. Observations of volcanic earthquakes and tremor at Deception Island, Antarctica, *Annali di Geofisica,* **42,** 417–436.

Almendros, J., Ibáñez, J.M., Alguacil, G., Del Pezzo, E. & Ortiz, R., 1997. Array tracking of the volcanic tremor source at Deception Island, Antarctica, *Geophys. Res. Lett.,* **24,** 3069–3072.

Baker, P.E., McReath, I., Harvey, M.R., Roobol, M.J. & Davies, T.G., 1975. *The geology of the South Shetland Islands: volcanic evolution of Deception Island,* Scientific Reports, British Antarctic Survey.

Barclay, A.H., Wilcock, W.S.D. & Ibáñez, J.M., 2009. Bathymetric constraints on the tectonic and volcanic evolution of Deception Island Volcano, South Shetland Islands, *Antart. Sci.,* **21**(2), 153–167.

Ben-Zvi, T., Wilcock, W.S.D., Barclay, A.H., Zandomeneghi, D., Ibáñez, J.M. & Almendros, J., 2009. The P-wave velocity structure of Deception Island, Antarctica, from two-dimensional seismic tomography, *J. Volc. Geotherm. Res.,* **180,** 67–80.

Carmona, E., Almendros, J., Serrano, I., Stich, D. & Ibáñez, J., 2012. Results of seismic monitoring surveys of Deception Island volcano, Antarctica, from 1999–2001, *Antart. Sci.,* **24,** 485–499.

Catalan, M., Agudo, L.M. & Muñoz-Martin, A., 2006. Geomagnetic secular variation of Bransfield Strait (western Antarctica) from analysis of marine crossover data, *Geophys. J. Int.,* **165,** 73–86.

Del Pezzo, E., 2008. Earth Heterogeneity and Scattering Effects of Seismic Waves: Seismic wave scattering in volcanoes, *Adv. Geophys.,* **50,** 353–371.

Fernandez-Ibáñez, F., Perez-Lopez, R., Martinez-Diaz, J.J., Paredes, C., Giner-Robles, J.L., Caselli, A.T. & Ibáñez, J.M., 2005. Costa Recta beach, Deception Island, West Antarctica: a retreated scarp of a submarine fault? *Antarct. Sci.,* **17,** 418–426.

García-Yeguas, A., Almendros, J., Abella, R. & Ibáñez, J.M., 2011. Quantitative analysis of seismic wave propagation anomalies in azimuth and apparent slowness at Deception Island volcano (Antarctica) using seismic arrays, *Geophys. J. Int.,* **184,** 801–815.

Gasparini, R. & TomoVes Working Group, 1998. Looking inside Mt. Vesuvius, *EOS, Trans. Am. geophys. Un.,* **79,** 229–236.

Hoshiba, M., 1993. Separation of scattering attenuation and intrinsic absorption in Japan using the multiple lapse time window analysis of full seismogram envelope, *J. geophys. Res.,* **98**(B9), 15 809–15 824.

Ibáñez, J.M., Del Pezzo, E., Almendros, J., La Rocca, M., Alguacil, G., Ortiz, R. & García, A., 2000. Seismovolcanic signals at Deception Island volcano, Antarctica: wave field analysis and source modeling, *J. geophys. Res.,* **135,** 13 905–13 931.

Ibáñez, J.M., Almendros, J., Carmona, E., Martínez-Arévalo, C. & Abril, M., 2003. The recent seismo-volcanic activity at Deception Island volcano, *Deep Sea Res. II,* **50,** 1611–1629.

Ibáñez, J.M., Rietbrock, A. & García-Yeguas, A., 2008. Imaging an Active Volcano Edifice at Tenerife Island, Spain, *EOS, Trans. Am. geophys. Un.,* **89**(32), 289–300.

La Rocca, M., Del Pezzo, E., Simini, M., Scarpa, R. & De Luca, G., 2001. Array analysis of seismograms from explosive sources: evidence for surface waves scattered at the main topographical features, *Bull. seism. Soc. Am.,* **91,** 219–231.

Lees, J.M. & Crosson, R.S., 1989. Tomographic inversion for three-dimensional velocity structure at Mount St. Helens using earthquake data, *J. geophys. Res.,* **94**(B5), 5716–5728.

Luzón, F., Almendros, J. & García Jerez, A., 2011. Shallow structure of Deception Island volcano, Antarctica, from correlations of ambient seismic noise on a dense set of seismic arrays, *Geophys. J. Int.,* **185,** 737–748.

Martí, J., Vila, J. & Rey, J., 1996. Deception Island (Bransfield Strait, Antarctica): an example of volcanic caldera developed by extensional tectonics, in *Volcanic Instability on the Earth and Other Planets,* Vol. 110, pp. 253–265, ed. McGuire, W.J., Geol. Soc. Spec. Publ.

Martínez-Árevalo, C., Bianco, F., Ibáñez, J.M. & Del Pezzo, E., 2003. Shallow seismic attenuation and shear-wave splitting in the short period range of Deception Island volcano (Antarctica), *J. Volc. Geotherm. Res.,* **128,** 89–113.

Mayeda, K., Koyanagi, S., Hoshiba, M., Aki, K. & Zheng, Y., 1992. A comparative study of scattering, intrinsic, and coda Q^{-1} for Hawaii, Long Valley and Central California between 1.5 and 15 Hz, *J. geophys. Res.,* **97,** 6643–6659.

Muñoz-Martin, A., Catalan, M., Martin, J. & Carbo, A., 2005. Upper crustal structure of Deception Island area (Bransfield Strait, Antarctica) from gravity and magnetic modelling, *Antarc. Sci.,* **17,** 213–224.

Onizawa, S. *et al.,* 2007. P-wave velocity structure of Usu volcano: implications of structural controls on magma movements and eruption locations, *J. Volc. Geotherm. Res.,* **160,** 175–194.

Ortiz, R., 1997. Monitoring of the volcanic activity of Deception Island, South Shetland Islands, Antarctica (1986–1995), in *The Antarctic Region: Geological Evolution and Processes,* pp. 1071–1076, ed. Ricci, C.A. *et al.,* Terra Antarctica Publishers.

Patanè, D., Barberi, G., Cocina, O., De Gori, P. & Chiarabba, C., 2006. Time-resolved seismic tomography detects magma intrusions at Mount Etna, *Science,* **313,** 821–823.

Pedrera, A., Ruíz-Constán, A., Heredia, N., Galindo-Zaldivar, G., Bohoyo, F., Marín-Lechado, C., Ruano, P. & Somoza, L., 2012. The fracture system and the melt emplacement beneath the Deception Island active volcano, South Shetland Islands, Antartica, *Antarc. Sci.,* **24,** 173–182.

Prudencio, J., Del Pezzo, E., García-Yeguas, A. & Ibáñez, J., 2013. Spatial distribution of intrinsic and scattering seismic attenuation in active volcanic islands, I: model and the case of Tenerife Island, *Geophys. J. Int.,* doi:10.1093/gji/ggt361.

Rowan, L.R. & Clayton, R.W., 1993. The three dimensional structure of Kilauea Volcano, Hawaii, from traveltime tomography, *J. geophys. Res.,* **98,** 4355–4375.

Ryzhik, L.V., Papanicolaou, G.C. & Keller, J.B. 1996. Transport equation for elastic and other waves in random media, *Wave Motion,* **24,** 327–370.

Saccorotti, G., Almendros, J., Carmona, E., Ibáñez, J.M. & Del Pezzo, E., 2001. Slowness anomalies from two dense seismic arrays at Deception Island volcano, Antarctica, *Bull. seism. Soc. Am.,* **91,** 561–571.

Sato, H. & Fehler, M., 1998. *Seismic Wave Propagation and Scattering in Heterogeneous Earth,* 1st ed., Springer-Verlag, 308 pp.

Shimizu, H. & Explosion Seismic Research Group of Unzen Volcano, 1997. Subsurface structure of Unzen volcano derived from the 1995 explosion experiment (in Japanese with English abstract), *in Proceedings of DPRI Symposium on Magma Exploration,* pp. 9–15.

Smellie, J.L., 2001. Lithostratigraphy and volcanic evolution of Deception Island, South Shetland Islands, *Antarct. Sci.,* **13,** 188–209.

Smellie, J.L., Lopez-Martinez, J. & Thomson, J.W., 2002. *Geology and Geomorphology of Deception Island,* British Antarctic Survey.

Somoza, L., Martinez-Frias, J., Smellie, J.L., Rey, J. & Maestro, A., 2004. Evidence for hydrothermal venting and sediment volcanism discharged after recent short-lived volcanic eruptions at Deception Island, Bransfield Strait, Antarctica, *Mar. Geol.,* **203,** 119–140.

Tomatsu, T., Kumagai, H. & Dawson, P.B., 2001. Tomographic inversion of P-wave velocity and Q structure beneath the Kirishima volcanic complex, southern Japan, based on finite difference calculations of complex traveltimes, *Geophys. J. Int.,* **146,** 781–794.

Vila, J., Martí, J., Ortiz, R., García, A. & Correig, A.M., 1995. Attenuation and source parameters at Deception Island (South Shetland Islands, Antarctica), *Pure appl. Geophys.,* **144,** 229–250.

Voight, B. *et al.,* 2010. Active source seismic experiment peers under Soufriére Hills Volcano, *EOS, Trans. Am. geophys. Un.,* **91**(28), 245.

Wegler, U., 2003. Analysis of multiple scattering at Vesuvius volcano, Italy, using data of the TomoVes active seismic experiment, *J. Volc. Geotherm. Res.,* **128,** 45–63.

Wegler, U., 2004. Diffusion of seismic waves in a thick layer: theory and application to Vesuvius volcano, *J. geophys. Res.,* **109,** doi:10.1029/2004JB003048.

Wegler, U. & Lühr, B.G., 2001. Scattering behaviour at Merapi Volcano (Java) revealed from an active seismic experiment, *Geophys. J. Int.,* **145,** 579–592.

Yamamoto, M. & Sato, H., 2010. Multiple scattering and mode conversion revealed by an active seismic experiment at Asama volcano, Japan, *J. geophys. Res.,* **115,** B07304, doi:10.1029/2009JB007109.

Zandomeneghi, D., 2007. Passive and active seismic tomography of volcanic islands Sao Miguel (Portugal) and Deception (Antarctica), *PhD thesis,* Universidad de Granada, Spain.

Zandomeneghi, D., Almendros, J., Ibáñez, J.M. & Saccorotti, G., 2008. Seismic tomography of Central Sâo Miguel, Azores, *Phys. Earth planet. Inter.,* **167,** 8–18.

Zandomeneghi, D., Barclay, A.H., Almendros, J., Ibáñez, J.M., Wilcock, W.S.D. & Ben-Zvi, T., 2009. Crustal structure of Deception Island volcano from P-wave seismic tomography: tectonic and volcanic implications, *J. geophys. Res.,* **114,** B06310, doi:10.1029/2008JB005599.

Zeng, Y., Su, F. & Aki, K., 1991. Scattering wave energy propagation in a random isotropic scattering medium: 1. Theory, *J. geophys. Res.,* **96,** 607–619.

Zollo, A. *et al.*, 1998. An image of Mt Vesuvius obtained by 2D seismic tomography, *J. Volc. Geotherm. Res.,* **82,** 161–173.